ISIJ International, Vol. 55 (2015), No. 9, pp. 1942–1949

Detection of Periodic Defects Using Dual-Light Switching Lighting Method on the Surface of Thick Plates

Yong-Ju JEON,[1] Doo-chul CHOI,[1] Jong Pil YUN[2] and Sang Woo KIM[1]*

1) Department of Electrical Engineering, POSTECH, Pohang, 790-784 South Korea.
2) System Research Group, Engineering Research Center, POSCO, Pohang, 790-784 South Korea.

(*Received on January 29, 2015; accepted on May 18, 2015*)

Currently, automated inspection algorithms are widely used to ensure high-quality products and achieve high productivity in the steel making industry. In this paper, we propose a vision-based method to detect periodic defects in the surface of thick plates. To minimize the influence of a non-uniform surface property and improve the accuracy of the detection rate, a detection method based on dual-light switching lighting (DLSL) proposed. In general, single lighting (SL) methods cannot well represent the steel surface because the surface features are not uniform and strongly vary according to lighting conditions. In the DLSL method, defective regions are represented by a black and white pattern, regardless of shape, size, or orientation. Therefore, defects can be found by the black and white patterns in the corresponding images. Gabor filtering was used to find defective regions and reduce the false positive rates. To find the periodic candidates of defects, we process the period searching using manufacturing information. To identify periodic defects from among the defect candidates, we use "similarity of shapes" features with a support vector machine (SVM) classifier. The experimental results show that the proposed algorithm is effective at detecting periodic defects on the surface of thick plates.

KEY WORDS: quality control; machine vision; surface inspection; defect detection; thick plate.

1. Introduction

In recent years, the steel making industry has expended significant effort on meeting the quality standards of customers. In order to remain competitive, steel companies aim to achieve not only high productivity but also high product quality. However, steel manufacturing processes create a difficult environment for defect inspection because of the hot-rolling processes that involve continuous casting and rolling. Therefore, many inspection steps are manually performed by humans[1] or occasional inspections.

In steel manufacturing conditions, many methods have been developed to improve the quality of steel and achieve automatic inspection. In this introduction, we briefly mention the various inspection techniques that have been developed for steel manufacturing environments, which include ultrasonic detection methods for stainless steel spot welds[2] and ductile iron,[3] quality monitoring using voltage signals for small-scale resistance spot welding,[4] 3D X-ray tomography inspection for fatigue in aluminum die castings,[5] and optical inspection techniques for slabs,[6,7] steel bar,[8,9] billets,[10] and silicon steel.[11] Although the several studies mentioned above have achieved good performance and can effectively detect their respective defects, it is difficult to apply them directly to defect detection in thick plate surfaces because each of these methods is optimized for a specific type of defect and material.

In this study, we propose a new detection method based on visual inspection techniques. Dual-light switching lighting (DLSL) is a method of image acquisition that uses switched lighting techniques. Generally, automated visual inspections use a single lighting (SL) method that consists of one camera and one lighting module. SL visual inspection has been applied in various industries such as textiles,[12–14] LCD panels,[15,16] and circuits[17] for its fast speed and diagnostic capabilities.[18] However, steel surfaces can have many uneven surface properties caused by non-uniform surfaces and scales, which are composed of oxidized substances caused during hot-process manufacturing. These scales are not a defined color or shape. In the SL case, uneven surface properties such as scales reflect light differently, making it difficult to detect the defects among them. In order to address this problem, we propose the DLSL method and describe its application to periodic defect detection on the surface of thick plate. To reduce the effect of scales, in the DLSL method, we find defective regions using the Gabor filtering method. To distinguish periodic defects from false positives, we search for and classify periodic defects using "similarity of shapes" features.

The rest of this paper is organized as follows. The DLSL method and target defect analysis are presented in Section 2. A detailed description of the proposed algorithms is presented in Section 3. The experimental results and conclusions are presented in Sections 4 and 5, respectively.

* Corresponding author: E-mail: swkim@postech.edu
DOI: http://dx.doi.org/10.2355/isijinternational.ISIJINT-2015-053

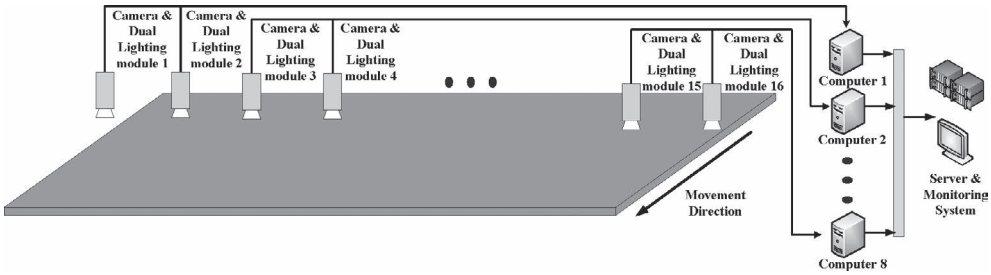

Fig. 1. Surface defect detection system.

2. Image Acquisition System and Target Defects

The thick plate surface images used in this study were directly acquired from an actual production line. Because the thick plates are hot steel plates that are transferred by rollers, we use line-scan cameras and horizontal arrays of cyan LEDs for the lighting source. **Figure 1** shows the detection system for the thick plates. The thick plates have various widths depending on production conditions. Therefore, sixteen camera and lighting modules are set up to handle the wider plates. The left edge of the thick plate is always captured by camera 1, and the right edge is captured by camera 10–16, depending on the width of the plate. The right edge is automatically detected by a laser detection system. The vertical and horizontal resolution of the line-scan camera used in this system are 0.25 mm, respectively. A frame grabber acquires 2 000 lines per frame, and one line consists of 2 048 pixels. Therefore, a captured frame from one camera has 2 048 × 2 000 pixels.

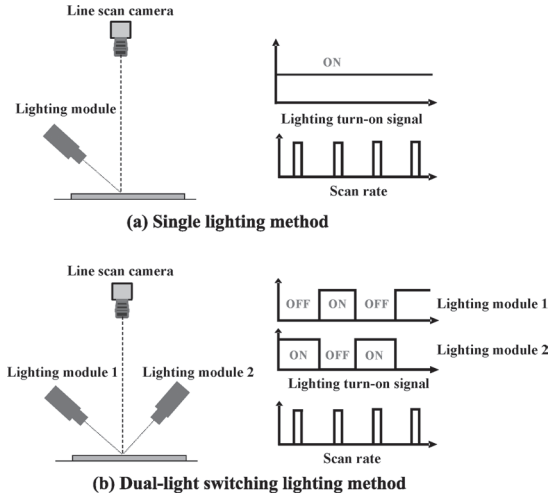

Fig. 2. Architecture of the lighting methods.

2.1. DLSL Method

To achieve good inspection algorithm performance, good lighting methods are essential. Our objective was to develop a detection algorithm that satisfactorily identified various defect shapes. The surface properties of the defective regions vary depending on various factors, such as the type of steel and manufacturing conditions. Therefore, defects have individual characteristics including size and shape. To address this issue, we proposed the DLSL method. **Figure 2**(a) shows the architecture of the SL method. The lighting module in the SL method is always activated, regardless of the scan rate. In this case, objects are always illuminated from one side. Therefore, various defect illumination patterns appear, depending on the defect direction, size, and thickness. In contrast, the DLSL method consists of one camera module and two lighting modules, as illustrated in Fig. 2(b). The two lighting modules are set up opposite each other on either side of the object, and each lighting module has an inverted on-off cycle that depends on the scan rate. Therefore, odd scan lines are illuminated by lighting module 1, and even scan lines are illuminated by lighting module 2. Because the two lighting modules are set up opposite each other at the same angle, the appearance of the normal surface does not change, as compared to the SL method. However, when the surface is lumpy, a black and white pattern appears because of the differently illuminated patterns generated by the on/off lighting cycle.

Figure 3 shows different sizes and shapes of defects. In the SL case, different illumination patterns are generated depending on the size, orientation, and shape of the defect. However, in the DLSL case, only black and white patterns in the defect areas are observed, regardless of the size, orientation, or shape of the defect. Therefore, when the DLSL method is used, detection problems related to the various sizes, orientations, and shapes of the defects can easily be solved by determining the black and white pattern regions. This is the strongest advantage of DLSL over SL, making it easier to solve fault detection problems.

2.2. Target Defects

In this paper, we propose an automated visual inspection system for the detection of hot leveler (HL) marks in thick plates. HL is a quality improvement process that is the final step in thick-plate manufacturing. In the HL rolling process, thick plate becomes flatter. **Figure 4** shows the HL rolling process. When damage occurs on the HL roller surface caused by the adhesion of foreign materials or by cracks in the roller itself, the thick plate surfaces are also damaged by the rolling process (Fig. 4). These defects are called HL mark defects (HLMDs). Because the HL process is a rolling process, HLMDs occur consecutively and periodically in the thick plate surface. When HLMDs are not detected quickly, a large quantity of defects can be generated in the thick plate surface. Hence, it is important to quickly detect HLMDs on the thick plate surface to maintain the quality of the final product.

Figure 5 shows images of HLMDs of various shapes and sizes. We have summarized several characteristics of

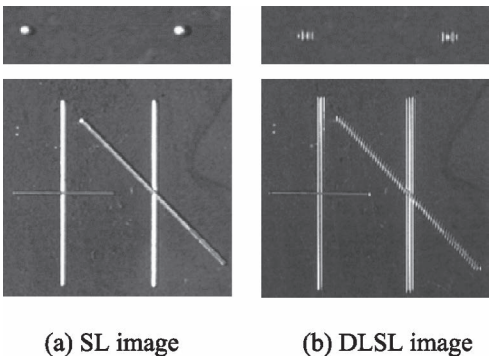

Fig. 3. Artificial defect images acquired under different lighting conditions.

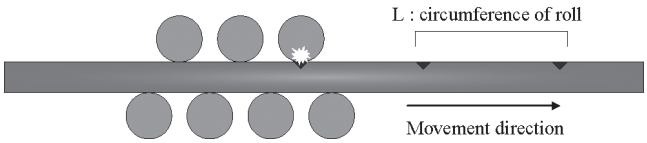

Fig. 4. HL roll process with damaged roll.

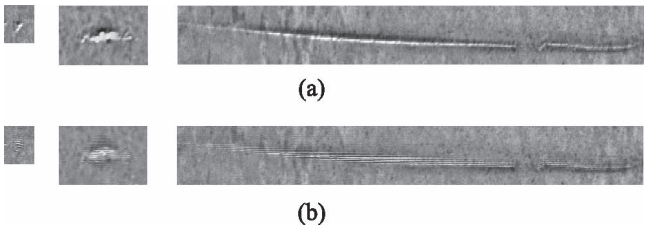

Fig. 5. Various shapes and sizes of HLMDs: (a) SL images and (b) DLSL images.

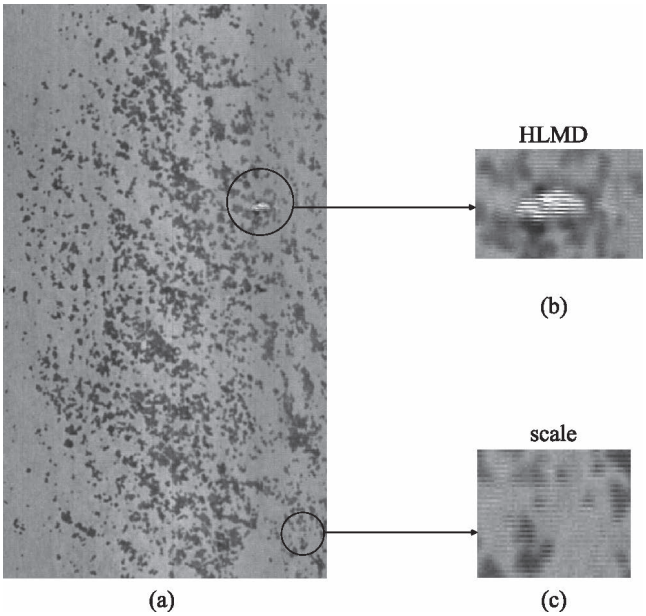

Fig. 6. Thick plate surface image acquired by DLSL methods: (a) image of thick plate surface with HLMD and scales, (b) enlarged region of the image containing an HLMD, and (c) region of the image that contains scales.

HLMDs from the statistical analysis of a large number of samples.

(1) HLMDs can occur anywhere on a thick plate surface and have various sizes and shapes depending on the type of damage to the rollers. The smallest HLMD size is 2–3 mm (8–12 pixels), and the largest HLMD size is the width of the roll. To identify the various HLMD sizes, accurate pattern extraction techniques are required.

(2) When HLMDs occur once, they occur consecutively and periodically in the thick plate surface with the same size and shape. The HLMDs are generated in the same vertical direction with period L, where L (Fig. 4) is the circumference of the roll. Therefore, a periodic check must be included to detect HLMDs and the similarity of the shape must also be checked. In other words, for accurate detection, it is necessary to determine a periodic HLMD group in thick plate surface through continuous observation.

In the next section, we provide a step-by-step description of the HLMD detection algorithm.

3. Defect Detection Algorithm

In this section, we develop an efficient algorithm to detect HLMD candidates in thick plates. HLMDs cause black and white patterns when DLSL is used. However, the main obstacle to HLMD detection is caused by scale (thin oxidation layers of the thick plate surface caused during hot-process manufacturing). **Figure 6**(a) shows images of the thick plate surface covered by scales. These scales can occur anywhere on the thick plate surface and be various colors and shapes. These scales do not affect the typical quality of the thick plate. However, swollen scales (Fig. 6(c)) also generate a weak black and white pattern in DLSL method, and these scales must be distinguished from HLMDs by the inspection algorithm. To improve the detection algorithm, we propose a three-step algorithm as follows. First, it determines the black and white patterns using Gabor filtering of the DLSL image. Second, it extracts candidate HLMDs by periodic searches. Finally, it classifies the candidates as HLMDs or scales using similarity of shape features.

3.1. Filtering for Pattern Extraction

The Gabor filter is an efficient filtering method in image processing. Because of its comprehensive filter design, the Gabor filter has been widely used for defect detection applications.[6,7,19–21] An important property of Gabor filters is that they achieve optimal joint localization (or resolution) in both the spatial and frequency domains.[22] In the spatial domain, the Gabor function is a complex exponential modulated by a Gaussian function. The general form of the two-dimensional (2D) Gabor function is given by:

$$G(x,y)=\frac{1}{2\pi\sigma_x\sigma_y}exp\left[-\frac{1}{2}\left(\frac{x^2}{\sigma^2{}_x}+\frac{y^2}{\sigma^2{}_y}\right)\right]exp\left(j2\pi fx\right) \quad \ldots (1)$$

Equation (1) can be split into a real part and an imaginary part. The real part of the 2D Gabor function acts as a blob detector, while the imaginary part acts as an edge detector.[23] Because HLMDs are area-type defects consisting of black and white patterns, the real part was applied in this method. The real form of the 2D Gabor function is given by:

$$g(x,y)=\frac{1}{2\pi\sigma_x\sigma_y}exp\left[-\frac{1}{2}\left(\frac{x'^2}{\sigma^2{}_x}+\frac{y'^2}{\sigma^2{}_y}\right)\right]\cos\left(2\pi fx'\right) \quad \text{.... (2)}$$

where $x' = xcos\theta + ysin\theta$ and $y' = -xsin\theta + ycos\theta$.

The Gabor filter is designed by selecting four parameters: θ denotes the rotation parameter, f denotes the radial frequency of the Gabor function, and the space constants σ_x and σ_y define the Gaussian envelope along the x and y axes, respectively. In this paper, Gabor designing focusses on the characteristics of HLMDs. Because the thick plate is transferred by rollers, the direction of movement is vertical with respect to the images. Therefore, continuous thick plate surface images are captured by line scan cameras along the vertical direction, and black and white patterns are represented by the scan rate with respect to the vertical direction (Fig. 6(b)). To extract the black and white patterns, f is set to 2 (the period of the black and white pattern is 2 pixels) and θ is set to 90°. Parameters σ_x and σ_y represent the bandwidth along the x and y axes, respectively, and are determined considering the size of the defects. To cover the smallest HLMD (8–12 pixels), σ_x and σ_y are set to 3. The Gabor filter itself is 9 × 9 pixels. The Gabor filter output $R(x, y)$ is defined as follows:

$$R(x,y)=g(x,y)*I(x,y)=\sum_{m=0}^{M-1}\sum_{n=0}^{N-1}g(m,n)I(x-m,y-n) \quad \text{... (3)}$$

where (*) denotes 2D convolution, $I(x, y)$ is the gray image acquired by the DLSL method, and $M \times N$ is the size of the Gabor filter. The energy of the filtered image $E(x, y)$ is calculated by the nonlinear square operator $|\cdot|^2$:

$$E(x,y)=\left|R(x,y)\right|^2 \quad \text{..... (4)}$$

Figures 7(b) and 7(c) show an image obtained using a Gabor filter that amplifies the HLMD region. Using the energy of the Gabor filtered image, we performed binarization with an adaptive threshold value. Because the HLMD region has a black and white pattern, the energy of the Gabor filtered output value in the HLMD region is always greater than the mean value of normal surface regions. To reduce the irregular image properties caused by scales, the adaptive threshold value was calculated using second-order statistics:

$$T=mean[E(x,y)]+\alpha\cdot std[E(x,y)] \quad \text{..... (5)}$$

where α is the weighting factor experimentally selected using a large number of samples. Because the $E(x, y)$ is energy of the Gabor filtered image from one-frame region, the value T is adaptively changed depending on the surface property. The binary image $B(x, y)$ is given by:

$$B(x,y)=\begin{cases}1, & E(x,y)>T\\ 0, & otherwise\end{cases} \quad \text{..... (6)}$$

Figure 7(d) shows the result of binarization on the HLMD.

3.2. Periodic Defect Candidate Selection

The proposed algorithm provides detecting periodic defects in thick plates. In the filtering stage, black and white pattern regions are extracted that include the HLMD regions. However, the scales in the thick plate surface can generate false positives. Therefore, to increase the performance of the inspection algorithm, a periodic search procedure must be included. To find candidates for periodic defects, we use only the position information of the detected blobs. **Figure 8** shows an example defect map that consists of detected blobs. The thick plate surface may have many noisy factors that consist of both scales and non-uniform surface regions. Therefore, the defect map consists of both true and false positives. The goal of the periodic search is

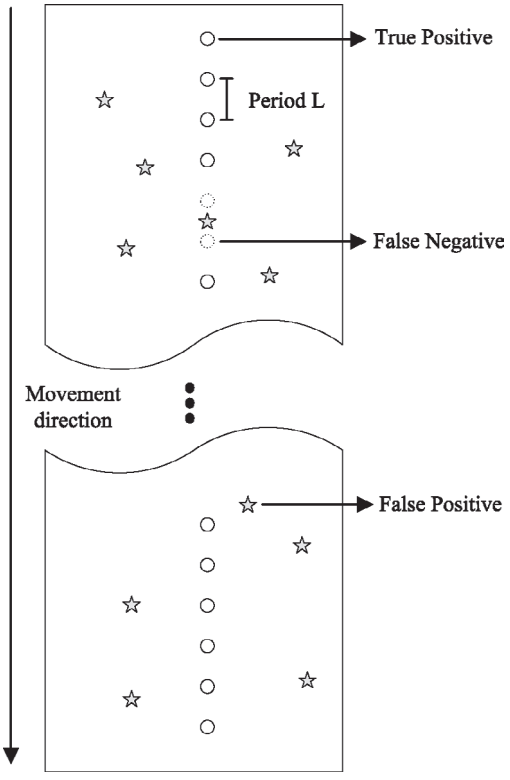

Fig. 8. Defect map. Circles are true positives, dotted circles are false negatives, and stars are false positives.

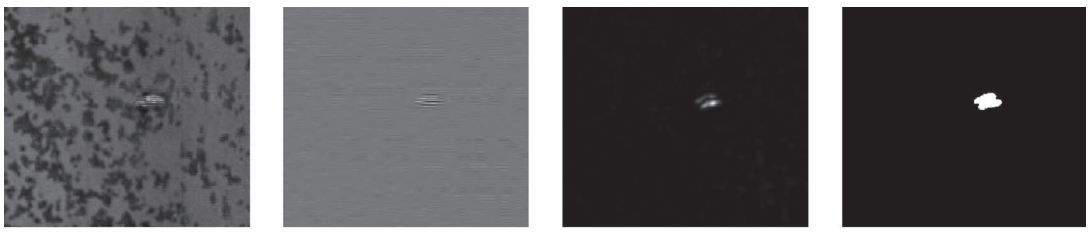

(a) (b) (c) (d)

Fig. 7. Step-wise result of binarization: (a) thick plate surface image with HLMD and scales, (b) result of Gabor filtering, (c) Gabor energy image, and (d) binary image.

to determine which candidates are periodic defects from among the detected false positives.

Because HLMDs are generated by roller damage, HLMD period L is equal to the outer circumference of the roll (Fig. 4). Moreover, a damaged roll generates the HLMDs in the same position in the rolling direction (Fig. 8). Therefore, to detect periodic defects, we partitioned the defect map region along the horizontal direction (**Fig. 9**). The sub-search region width is σ_w and the sliding interval is $S_w = \sigma_w/2$. When the image width is W, $W/S_w - 1$ search regions are generated. The σ_w can be changed from 1 to W. The large σ_w generates a small number of the search regions, it is excellent for processing speed, but many noise components are including in search regions. Therefore, the detection rate of small defects is reduced. On the other hand, small σ_w generates a large number of the search regions, the processing time is increased, and the accuracy of period detection for small defects is increased. Therefore, we consider for small size of defects, σ_w is experimentally determined to 64 pixels.

Figure 9 shows the sub-search region division and the corresponding position vector $H_i(n)$ in the ith sub-search region, where $n = 0,1,2, ..., N-1$. We compensate for the uncertainty of defect position, dividing the length of defect map into N equally spaced bins of L_{bin} along vertical direction. The number of bins N is $N = L_{plate}/L_{bin}$, where L_{plate} is size of thick plate along vertical direction and L_{bin} is bin size. Therefore, the size of position vector $H_i(n)$ is N. In this paper, we consider for small size of defects, L_{bin} is experimentally determined to 10 pixels. The false positives are mainly caused by elements in the noisy background such as scales. These false positive results influence the performance of the inspection algorithm. To increase the detection rate, we detect the periodic occurrence of defects in position vector $H_i(n)$.

As mentioned, period L is known information. It is equal to the outer circumference of the roll, and is 880 mm (3 520 pixels). Therefore, we can simply create an artificial position vector $S_l(n)$ of period L (**Fig. 10**(b)). Position vector $H_i(n)$ includes both HLMD positions and false positive positions (Fig. 10(a)). To determine the sequences of period L, we calculate the correlation of $H_i(n)$ and $S_l(n)$ as follows:

$$y_i(n) = \sum_{k=0}^{N-1} H_i(k) S_n(k) \quad \text{..... (7)}$$

where N is the length of the position vector and $S_l(n)$ is defined as follows:

$$S_l(n) = \begin{cases} 1, & n = \{l, l+L, l+2L, l+3L, \cdots\} \\ 0, & \text{otherwise} \end{cases} \quad \text{..... (8)}$$

Because the HLMDs have period L, and $S_l(n)$ is artificial position vector of period L and shifted position l, the position of maximum correlation represents the start point of a candidate HLMD. Figure 10 illustrates the periodic search procedure. Position vector $H_i(n)$ includes HLMD positions with many noise factors (Fig. 10(a)). After correlation, output $y_i(n)$ (Fig. 10(c)) represents the correlated values. Because HLMDs have period L, the maximum value of $y_i(n)$ is equal to the start point of the HLMDs and large values

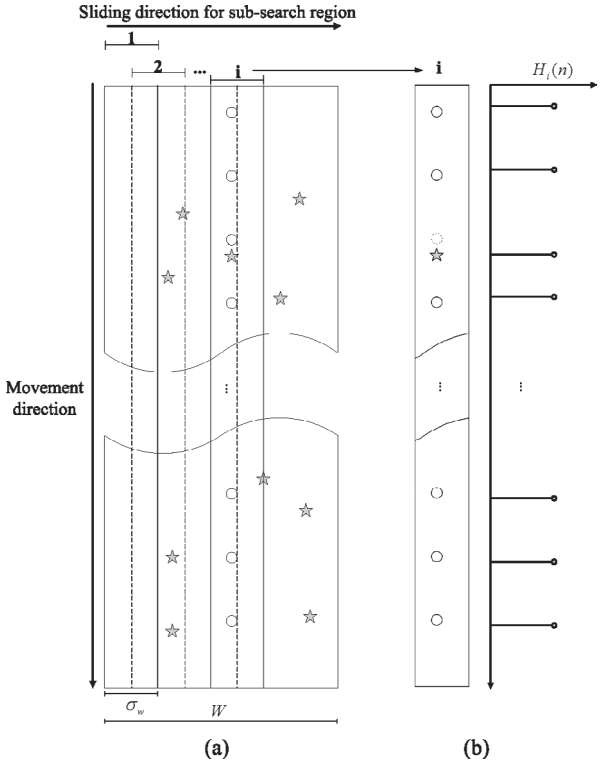

Fig. 9. Defect map with sub-search regions: (a) defect map partitioned into sub-search regions and (b) the ith sub-search region and corresponding position vector $H_i(n)$.

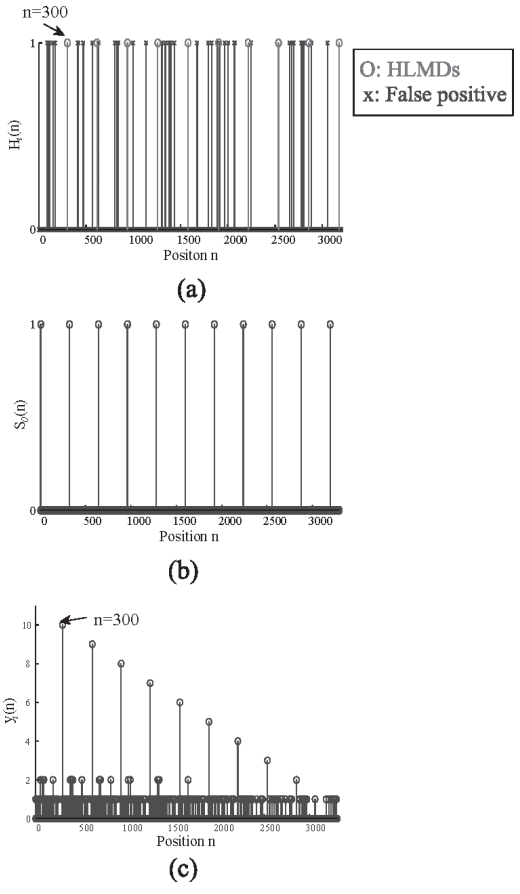

Fig. 10. Periodic defect identification procedure: (a) position vector $H_i(n)$ includes both HLMD and false positive positions with period L, (b) artificial position vector $S_0(n)$ with period L, and (c) output value $y_i(n)$.

appear repeatedly according to the period L. Therefore, we can simply chose the start point of the HLMDs, and select the candidates of HLMD groups. **Figure 11** shows the periodic defect candidate groups selected by the periodic search process.

3.3. Feature Extraction and Classification

Although the pattern extraction and periodic search process reduces false positive detections, the influence of pseudo-defects remains, caused by scales and noisy surfaces. In this section, we apply a classification process using the similarity of the periodic defects. The HLMDs are generated by damage to the same roll. Therefore, periodic HLMDs have the same shapes, orientations, sizes, and positions in the horizontal direction. To achieve high detection accuracy, we apply a support vector machine (SVM) learning algorithm that uses features extracted from the periodic defects.

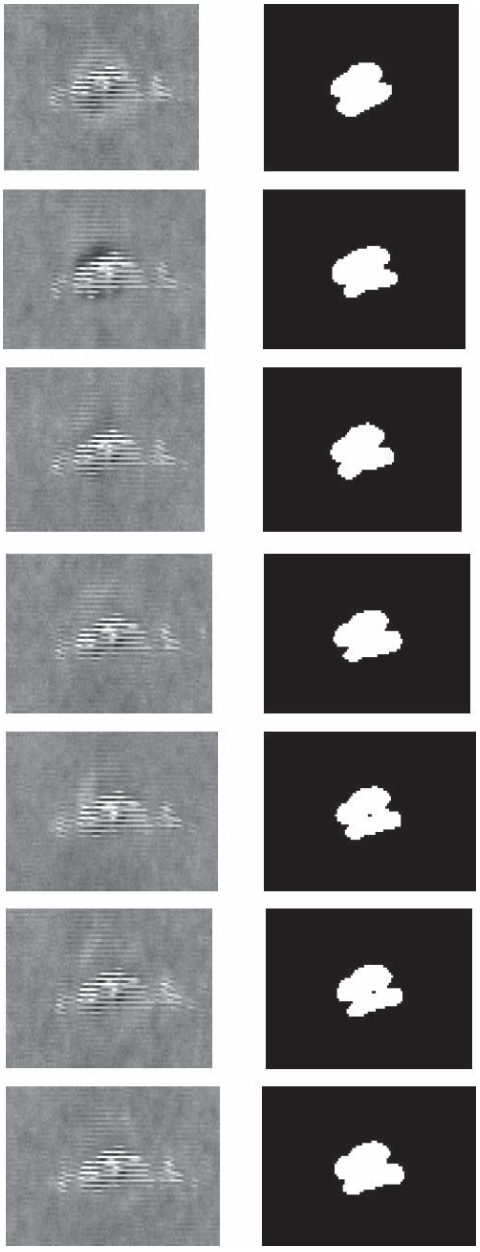

Fig. 11. HLMD periodic group images selected by the periodic search process in the same thick plate surface (DLSL images (left) and binary images (right)).

The ith candidate of a periodic defect consists of the set of detected blobs:

$$D_i = \{Blob_1^i(x,y), Blob_2^i(x,y), \cdots, Blob_M^i(x,y)\} \quad \text{..... (9)}$$

where M is the number of defects with the same period L and D_i is an HLMD or pseudo defect. To classify the HLMDs and the pseudo defects, we use the blob information. From the set of blob information, we can calculate the shape, orientation, and position features. HLMDs have the same overall shape as well as shape and position in the horizontal direction caused by roller damage from the same roll. Hence, the standard deviations (STDs) of the feature values must be small. Each feature is described in the following subsections.

3.3.1. Feature Extraction

Because HLMDs are generated by the same roller, HLMDs have same size and shape. In contrast, pseudo-defects are caused by scales or non-uniform properties of the thick plate surface. To distinguish the HLMDs from pseudo-defects, we use the following morphological features:

- *Area*
  The area represents the total number of pixels in the detected blobs. In HLMDs, detected blobs have similar areas. The blob area is given by:

$$A = \sum_{m=0}^{M-1}\sum_{n=0}^{N-1} B(m,n) \quad \text{..... (10)}$$

  where $B(x, y)$ is the blob binary image, and M × N is the size of $B(x, y)$.
- *Horizontal position*
  Given the blob information, we can calculate the horizontal coordinates of the center of gravity of a blob as follows:

$$g_x = \frac{C_{10}}{C_{00}} = \frac{\sum_{m=0}^{M-1}\sum_{n=0}^{N-1} mB(m,n)}{\sum_{m=0}^{M-1}\sum_{n=0}^{N-1} B(m,n)} \quad \text{..... (11)}$$

  where $B(x, y)$ is a blob binary image and M × N is the size of $B(x, y)$ and C_{ij} is the central moment of the binary blob, as defined by:

$$C_{ij} = \sum_{m=0}^{M-1}\sum_{n=0}^{N-1} m^i n^j B(m,n) \quad \text{..... (12)}$$

  Because HLMDs are generated by a single damaged roller, they occur at the same position in the horizontal direction.
- *Orientation and Elongation*
  Figure 12 shows an ellipse with the same normalized second central moments as a blob region. L_{major} is the length of the major axis of the ellipse, and L_{minor} is the length of the minor axis of the ellipse. Orientation θ is given by the angle of the major axis with respect to the horizontal axis:

$$\theta = -0.5 \arctan \frac{2C_{11}}{C_{20} - C_{02}} \quad \text{..... (13)}$$

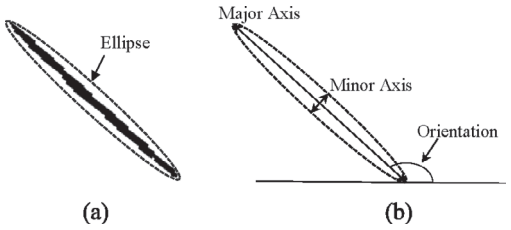

Fig. 12. (a) Ellipse with the same normalized second central moments and (b) major, minor axis, and orientation.

and the major and minor axis are calculated as follows:[24)]

$$C = \begin{pmatrix} \sigma_{xx} & \sigma_{xy} \\ \sigma_{yx} & \sigma_{yy} \end{pmatrix} \quad \text{..... (14)}$$

where

$$\sigma_{xx} = \frac{1}{A}\sum_{m=0}^{M-1}\sum_{n=0}^{N-1}(mB(m,n) - g_x)^2$$
$$\sigma_{yy} = \frac{1}{A}\sum_{m=0}^{M-1}\sum_{n=0}^{N-1}(nB(m,n) - g_y)^2 \quad \text{... (15)}$$
$$\sigma_{xy} = \sigma_{yx} = \frac{1}{A}\sum_{m=0}^{M-1}\sum_{n=0}^{N-1}(mB(m,n) - g_x)^2(nB(m,n) - g_y)^2$$

g_x, g_y is the centroid of the blob as defined by:

$$g_x = C_{10}/C_{00}, \quad g_y = C_{01}/C_{00} \quad \text{..... (16)}$$

The length of the two principal axes L_{major} and L_{minor} are equal the eigenvalues λ_1, λ_2 of the covariance matrix C, respectively.
Therefore,

$$\begin{cases} L_{\text{major}} = \lambda_1 = \frac{1}{2}\left[\sigma_{xx} + \sigma_{yy} + \sqrt{(\sigma_{xx} + \sigma_{yy})^2 - 4(\sigma_{xx}\sigma_{yy} - \sigma^2{}_{xy})}\right] \\ L_{\text{minor}} = \lambda_2 = \frac{1}{2}\left[\sigma_{xx} + \sigma_{yy} - \sqrt{(\sigma_{xx} + \sigma_{yy})^2 - 4(\sigma_{xx}\sigma_{yy} - \sigma^2{}_{xy})}\right] \end{cases}$$
..... (17)

The elongation can be calculated:

$$1 - \frac{L_{\text{minor}}}{L_{\text{major}}} \quad \text{..... (18)}$$

The HLMD candidates consist of the set of detected periodic blobs. Therefore, to check their similarity, we use the STD values of the feature set. A small STD represents similarity of shape and position for a set of periodic defects, and a large STD value represents dissimilarity. Because HLMDs have the same size, shape, and x-position, the STD values of the feature set are small compared to those of the pseudo-defects. **Figure 13** shows the STD values of the feature set. Here, HLMDs are well represented by small values.

3.3.2. Defect Classification

In this section, we classify the HLMDs using an SVM classifier. SVM is basically an approximate implementation of the method of structural risk minimization.[25,26)] The unique attribute of SVM is that it provides an excellent generalization performance on pattern classification problems in high dimensional spaces without the need to incorporate problem domain knowledge. Given a training set of instance-label pairs (x_i, y_i), $i = 1,2, \ldots, N$ where $x_i \in R^n$ and $y \in \{1, -1\}$, SVM constructs an optimal hyperplane to separate the training patterns into two classes with the margin of separation maximized. The equation of hyperplane $g(x)$ is

$$g(x) = \text{sgn}(w^T\phi(x) + b) \quad \text{..... (19)}$$

where b is the bias, w is the optimal weight vector, and ϕ is a mapping function that maps training or feature vector x_i into a higher dimensional space. SVM requires the solution of the following optimization problem:

$$\min(w, b, \xi) : \frac{1}{2}w^T w + C\sum_{i=1}^{N}\xi_i \quad \text{..... (20)}$$

subject to

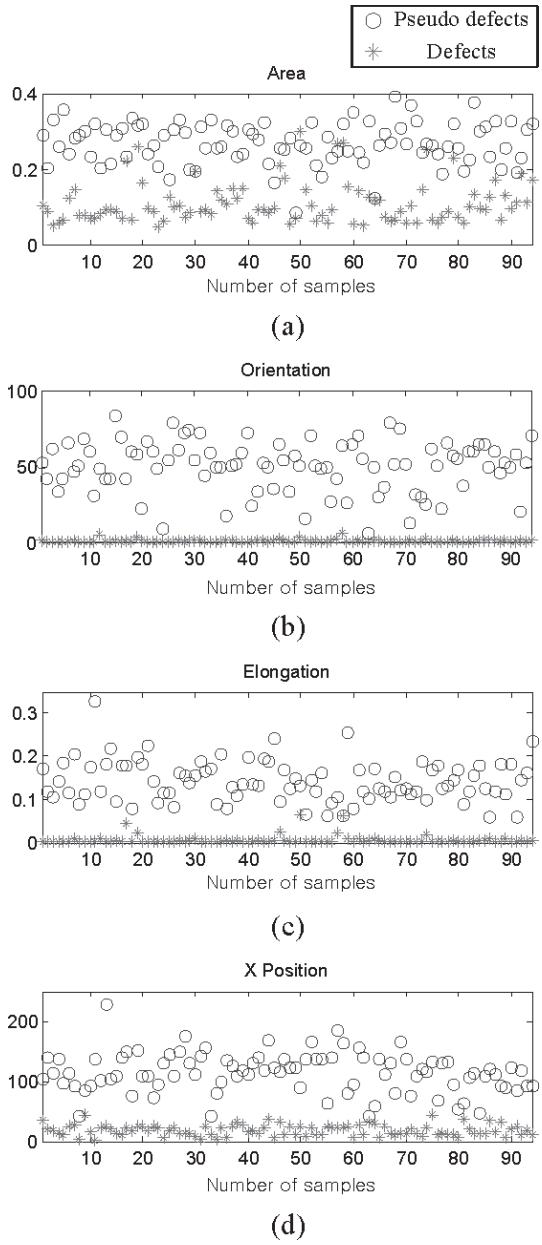

Fig. 13. STD values on the feature set: (a) area, (b) orientation, (c) elongation, and (d) position in the x direction (horizontal).

Table 1. Classification results using the SVM classifier.

	Defect	Normal
Training data	100.00% (47/47)	100.00% (754/754)
Test data	100.00% (47/47)	100.00% (754/754)
Accuracy	100.00% (94/94)	100.00% (1 508/1 508)

$$y_i(w^T\phi(x_i)+b) \geq 1-\xi_i \text{ and } \xi_i \geq 0 \quad \text{..... (21)}$$

where $C > 0$ is the penalty parameter, and ξ_i is a slack variable that incorporates non-separable data. Furthermore, $K(x_i,x_j) = \phi(x_i)^T\phi(x_j)$ is called the kernel function.

4. Experimental Results

To test detection performance, we prepared a thick plate surface image directly captured by the DLSL method from a real production line. A total of 1 602 candidate periodic defects were used to build the SVM classifier. The number of HLMDs was 94. The number of pseudo-data that were false detections cause by scales was 1 508. To evaluate the SVM classifier, 50% of the data were set aside to validate the performance of the classifier. Forty-seven HLMDs and 754 pseudo-data were used to training the SVM classifier. Each feature vector contained four STD values on the set of the features. The SVM kernel function adopted a radial basis function (RBF).[27] There are only two parameters to be determined in this SVM model: penalty parameter C and kernel parameter γ. To determine the best classification results, we performed a cross-validation and parameters C and γ were selected using grid search. **Table 1** summarizes the results of the classification.

In order to evaluate the performance of the proposed algorithm, we performed an experiment on 217 defect images and 2 010 normal images that were independent of the classification experiment. The proposed algorithm achieved 100.00% (217/217) accuracy for the detection of HLMDs with a false positive rate of 0.75% (15/2 010). Consequently, the proposed algorithm using the DLSL method and periodic search was effective at detecting HLMDs in the thick plate surface.

5. Conclusion

In this study, we developed an automated vision-based surface inspection method for thick plate. To enhance the features of defective regions compared to noisy surfaces, we proposed the DLSL method that makes it easier to solve fault detection problems by generating black and white patterns. The black and white patterns extracted by Gabor filtering and an adaptive thresholding method formed candidates of the periodic defect groups that were selected by a periodic search. To classify HLMDs and pseudo-defects, we proposed using shape similarity and classifying HLMDs and pseudo-defects using an SVM classifier. The proposed inspection algorithm was shown experimentally to be effective at detecting HLMDs in real thick plate surface images.

Acknowledgments

This research was supported by the MSIP(Ministry of Science, ICT and Future Planning), Korea, under the "IT Consilience Creative Program" (NIPA-2014-H0201-14-1001) supervised by the NIPA (National IT Industry Promotion Agency).

REFERENCES

1) X. Li, S. K. Tso, X. P. Guan and Q. Huang: *IEEE Trans. Ind. Electron.*, **53** (2006), 1927.
2) J. Liu, G. Xu, X. Gu, G. Zhou and Y. Hao: *ISIJ Int.*, **54** (2014), 1876.
3) W. Orłowicz, M. Tupaj and M. Mróz: *ISIJ Int.*, **50** (2010), 906.
4) D. Zhao, Y. Wang, Z. Lin and S. Sheng: *ISIJ Int.*, **53** (2013), 240.
5) Q. Wan, H. Zhao and C. Zou: *ISIJ Int.*, **54** (2014), 511.
6) S. G. Ryu, D. Choi, Y. J. Jeon, S. J. Lee, J. P. Yun and S. W. Kim: *ISIJ Int.*, **54** (2014), 112.
7) D. Choi, Y. J. Jeon, J. P. Yun and S. W. Kim: *Appl. Opt.*, **50** (2011), 5122.
8) W. Li, C. Lu and J. Zhang: *Appl. Surf. Sci.*, **258** (2012), 6080.
9) J. P. Yun, B. Seo and S. W. Kim: *Opt. Eng.*, **47** (2008), 077204.
10) Y. J. Jeon, D. Choi, S. J. Lee, J. P. Yun and S. W. Kim: *J. Opt. Soc. Am. A*, **31** (2014), 227.
11) K. C. Song, S. P. Hu, Y. H. Yan and J. Li: *ISIJ Int.*, **54** (2014), 2598.
12) S. C. Kim and T. J. Kang: *J. Opt. Soc. Am. A*, **23** (2006), 2690.
13) A. Kumar: *Pattern recognit.*, **36** (2003), 1645.
14) Y. Han and P. Shi: *Image Vis. Comput.*, **25** (2007), 1239.
15) C. J. Lu and D. M. Tsai: *Int. J. Adv. Manuf. Technol.*, **25** (2005), 53.
16) Y. C. Song, D. H. Choi and K. H. Park: *Jpn. J. Appl. Phys.*, **45** (2006), 5069.
17) J. J. C. Sanz and A. K. Jain: *J. Opt. Soc. Am. A*, **3** (1986), 1465.
18) R. T. Chin and C. A. Harlow: *IEEE Trans. Pattern. Anal. Mach. Intell.*, **PAMI-4** (1982), 557.
19) M. Ralló, M. S. Millán and J. Escofet: *J. Opt. Soc. Am. A*, **26** (2009), 1967.
20) D. M. Tsai and S. K. Wu: *Int. J. Adv. Manuf. Technol.*, **16** (2000), 474.
21) K. L. Mak and P. Peng: *Robot. Comput. Integr. Manuf.*, **24** (2008). 359.
22) J. L. Raheja, S. Kumar and A. Chaudhary: *Optik*, **124** (2013), 6469.
23) D. P. Casasent and J. S. Smokelin: *Opt. Eng.*, **33** (1994), 2255.
24) M. Yang, K. Kpalma and J. Ronsin: Pattern Recognition Techniques, Technology and Applications, IN-TECH, Croatia, (2008), 43.
25) B. E. Boser, I. M. Guyon and V. N. Vapnik: Proc. 5th Annual ACM Workshop on Computational Learning Theory, ACM Press, Pittsburgh, PA, (1992), 144.
26) C. J. C. Burges: *Data Min. Knowl. Discov.*, **2** (1998), 121.
27) B. Schölkopf, K. Sung, C. Burges, F. Girosi, P. Niyogi, T. Poggio and V. Vapnik: *IEEE Trans. Signal Process.*, **45** (1997), 2758.